Leak Localization and Orifice Diameter Estimation in Coal Mine Gas Drainage Pipelines Using a Physics-Informed Dual-Stream Decoupling Network

Weifeng Wang, Yu Zhang*, Li Tang, Bin Liu, Yu Shao, Jie Dong, Zhangkun Chen

School of Electrical and Control Engineering, Xi'an University of Science and Technology, Xi'an, China

Received 02 September 2026; revised 07 October 2026; accepted 12 October 2026

DOI: https://doi.org/10.46604/ijeti.2026.16761

Abstract

Leak localization and orifice diameter estimation involve different spatiotemporal scales, complicating joint prediction. This study aims to improve both tasks by constructing a multi-condition dataset from pressure, flow rate, and oxygen concentration signals and proposing a physics-informed dual-stream decoupling network (PI-DSDN). Its transient localization branch extracts multiscale pressure disturbances and uses a pressure-gradient energy mask to focus temporal attention on leakage transients. Its steady-state sizing branch decouples fast and slow variables and uses a macroscopic flow-rate difference to characterize post-leakage redistribution. On the test set, PI-DSDN achieves R^2 values of 0.9754 for localization and 0.9566 for sizing, with MAEs of 0.283 m and 0.0736 mm and RMSEs of 0.445 m and 0.1129 mm, respectively. Compared with CNN-LSTM, PI-DSDN reduces the localization and sizing MAEs by 45.2% and 45.1%, respectively. Ablation and attention analyses confirm that the physical priors selectively enhance transient localization and steady-state sizing, supporting more interpretable leak assessment.

Keywords: Coal mine gas drainage pipeline, leak localization, orifice diameter estimation, physics-informed learning, temporal attention

1. Introduction

Efficient extraction and utilization of coalbed methane are essential for ensuring safe coal mining and reducing methane emissions [1]. When a gas drainage pipeline operating under negative pressure develops a leak, ambient air is drawn into the pipeline, causing abnormal pressure, flow rate, and gas concentration. These changes can reduce drainage efficiency and create potential safety hazards. Accurate localization of the leak and quantitative estimation of its orifice diameter are therefore of considerable engineering importance.

Existing pipeline leak diagnosis methods can be broadly classified into three categories: physics-based methods, external sensing methods, and data-driven methods. Sekhavati et al. reviewed computational methods based on mass balance, negative pressure waves, and real-time transient models [2]. Zhang et al. localized leaks in gas drainage pipelines using changes in the pressure gradient before and after leakage [3]. Although these methods offer clear physical interpretations, they generally require accurate pipeline parameters, boundary conditions, and characterization of pressure propagation. External sensing methods detect leakage-induced acoustic, vibration, strain, or thermal responses. Acoustic detection, fiber Bragg grating vibration sensing, and vibration-temperature information fusion have been applied to leak detection and localization [4-6]. However, their performance in underground coal mines may be affected by mechanical vibration, environmental noise, and sensor installation constraints.

* Corresponding author. E-mail address: 24206206078@stu.xust.edu.cn

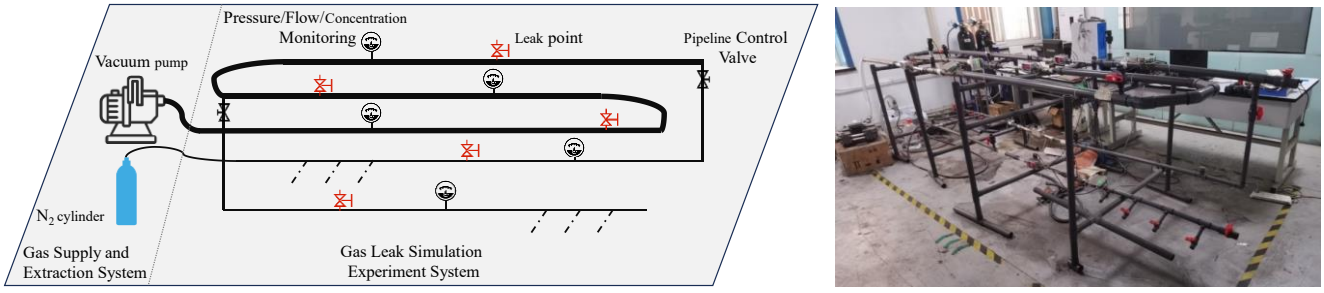
Data-driven methods have been increasingly applied to pipeline leak diagnosis. Existing studies have used multivariate temporal encoding, optimized neural networks, and multisource ensemble learning for leak detection and localization [7-9], while attention-based LSTM and spatiotemporal fusion models have improved feature extraction from multisensor time-series data [10, 11]. Li et al. combined enhanced external attention and multiscale denoising in a dual-stream Transformer for joint leak localization and orifice sizing [12]. Wu et al. constructed physics-aware gated attention from the temperature change rate and pressure gradient for leakage-state classification [13], whereas Keumoe et al. used synthetic multiparameter data and a random forest for leak-severity classification and online monitoring [14]. Physics-informed learning has also been applied to estimate leak location, intensity, and size [15, 16]. However, existing methods may not sufficiently distinguish the transient pressure propagation relevant to localization from the steady-state multiparameter evolution governing sizing, potentially leading to interference between features at different temporal scales.

To address this limitation, this study constructs a multi-condition coal mine gas drainage pipeline leakage dataset and proposes a physics-informed dual-stream decoupling network (PI-DSDN). Unlike the learnable gating of Transformer self-attention using physical variables [13], PI-DSDN applies a multipoint pressure-gradient energy mask exclusively to the transient localization branch, while fast-slow variable decoupling and a macroscopic flow-rate difference are used in the steady-state sizing branch. This task-specific design is intended to facilitate the joint prediction of leak location and orifice diameter. Baseline comparisons, ablation experiments, and attention analysis are conducted to evaluate its predictive performance and physical interpretability.

2. Gas Drainage Pipeline Leakage Experiments and Dataset Construction

2.1 Pipeline leakage experimental platform

To obtain the dynamic responses of pressure, flow rate, and oxygen concentration during pipeline leakage, a gas drainage pipeline leakage experimental platform was constructed. Its system configuration and physical setup are shown in Figs. 1(a) and 1(b), respectively. The platform consists of five subsystems: gas supply and extraction, pipeline transport, leak simulation, multiparameter monitoring, and data acquisition. The vacuum pump maintains a stable negative pressure. Considering the flammability and explosion risk of methane, inert N_2 was used to simulate the low-oxygen gas environment inside the pipeline. Under negative-pressure leakage conditions, both N_2- and methane-filled pipelines can exhibit pressure transients, flow redistribution, and changes in O_2 concentration due to ambient-air ingress, although differences in gas properties may affect the response magnitudes and propagation rates.



(a) Schematic diagram of the system (b) Photograph of the experimental platform

Fig. 1 Coal mine gas drainage pipeline leakage experimental platform

The main pipeline is constructed from PVC, with a total length of 13 m and an inner diameter of 50 mm. Elbows are incorporated to reproduce the nonideal flow conditions of practical pipeline networks. The vacuum-pump power setting is adjusted to establish different negative-pressure operating conditions, while the downstream control valve regulates the pipeline flow. Multiple controllable leak ports are distributed along the pipeline to simulate leaks at different locations and with different orifice diameters.

Three monitoring nodes are installed along the pipeline to synchronously measure pressure, flow rate, and oxygen concentration. When a leak occurs, ambient air enters the pipeline driven by the pressure difference between the interior and exterior, resulting in pressure disturbances, flow redistribution, and changes in oxygen concentration. The acquired signals are transmitted to a host computer through the data acquisition module and stored, providing the basis for constructing time-series samples and performing leak localization and orifice diameter estimation.

2.2 Leakage conditions and experimental design

To investigate the multi-parameter responses under different extraction and leakage conditions, a three-factor full-factorial experiment was conducted with the vacuum-pump power setting, leak orifice diameter, and leak location as the experimental factors. The vacuum-pump power setting was adjusted to 100%, 80%, and 60%, corresponding to high, medium, and low negative-pressure operating conditions, respectively. The relative leak location was defined as the ratio of the distance from the pipeline inlet to the leak point to the total length of the main pipeline. The experimental conditions are summarized in Table 1.

Table 1 Experimental conditions for pipeline leakage

Experimental factor	Setting
Vacuum-pump power setting	100% (high negative pressure), 80% (medium negative pressure), 60% (low negative pressure)
Leak orifice diameter (mm)	1.0, 1.5, 2.0, 2.5
Relative leak location	0.27, 0.46, 0.61, 0.88
Sampling frequency (Hz)	100

The full-factorial design comprised 48 leakage conditions. Twenty independent experimental runs were performed for each condition, resulting in a total of 960 leakage samples.

2.3 Physical anchor alignment and time-series sample construction

The occurrence time of a leakage event is uncertain in continuous monitoring sequences. The initial pressure transient and its first derivative contain the arrival-time information of negative pressure waves [17], while transient signal identification and time-delay estimation within continuous windows directly affect leak localization accuracy [18]. Dividing the sequence using a fixed stride may therefore truncate the pressure wavefront or place the transient at inconsistent positions across samples. To address this issue, the initial pressure change induced by leakage is defined as the physical anchor t_0, and different leakage events are aligned to a unified relative time coordinate.

The physical anchor is determined as follows. First, a moving average is applied to the pressure sequence to suppress local noise. A lagged difference is then calculated from the smoothed pressure sequence, and the peak absolute difference is used to obtain an initial estimate of the leakage disturbance. Finally, threshold detection relative to the local pre-leakage steady-state pressure baseline is applied to determine the exact onset time. The continuous multiparameter sequence is subsequently segmented using an asymmetric window:

$$X_i = X[t_0 - T_b,\ t_0 + T_a] \tag{1}$$

where $\boldsymbol{X}$ denotes the continuous multiparameter sequence, $\boldsymbol{X_i}$ is the sample corresponding to the *ith* leakage event, T_b is the background reference window before the anchor, and T_a is the dynamic response window after the anchor. In this study, T_b and T_a are set to 3.5 and 15.5 s, respectively, resulting in a fixed sample duration of 19.0 s. The pre-anchor interval represents the stable operating state before leakage, whereas the post-anchor interval covers pressure-disturbance propagation, flow-rate variation, and oxygen-concentration response. A typical aligned leakage sample is shown in Fig. 2.

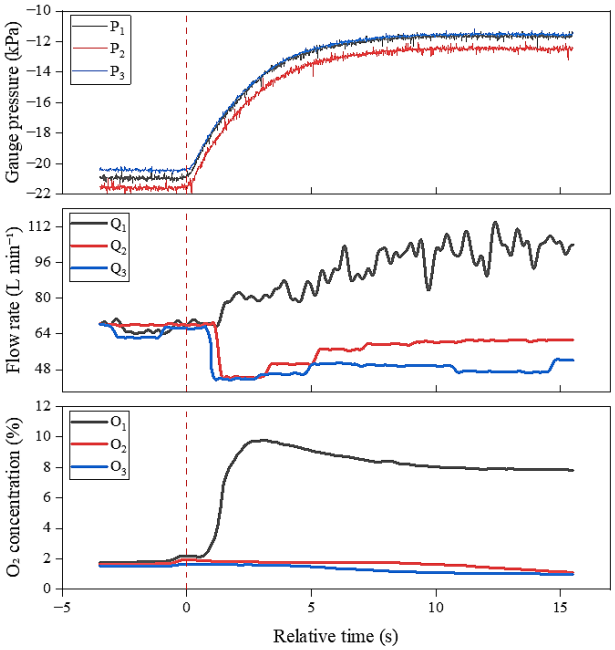


Fig. 2 Typical leakage time-series sample aligned using the physical anchor

As shown in Fig. 2, the pressure signals exhibit the earliest changes near t_0, followed by flow-rate and oxygen-concentration responses at different temporal scales. Compared with conventional sliding-window segmentation, the proposed method reduces the risk of critical transient information being attenuated or truncated due to window offsets, while retaining the pre-leakage steady state, leakage transient, and post-leakage evolution. It therefore provides consistently structured and temporally aligned samples for the subsequent localization and sizing branches.

2.4 Data preprocessing and dataset partitioning

To reduce the effects of differences in initial negative pressure, background flow rate, and baseline oxygen concentration among the extraction conditions, the baseline mean of each monitoring channel is calculated from the pre-leakage reference segment. The raw signals are then converted into relative changes:

$$x_{r,c}(t)=\frac{x_c(t)-x_{c,b}}{|x_{c,b}|+\varepsilon}\times 100\% \tag{2}$$

where $x_c(t)$ is the raw measurement of the *cth* physical channel at time *t*, $x_{c,b}$ is its mean over the pre-leakage reference segment, ε is a small positive constant that prevents division by zero, and $x_{r,c}(t)$ is the baseline-corrected relative change. This transformation suppresses differences in the initial steady states among operating conditions and highlights the dynamic responses induced by leakage.

The localization label is defined as the relative leak location $y_{loc}=L_\ell/L$, where L_ℓ is the distance from the pipeline inlet to the leak point and *L* is the total length of the main pipeline. The sizing label is defined using the ratio of the leak orifice area to the cross-sectional area of the main pipeline:

$$r=\frac{A_l}{A_p}=\left(\frac{d_l}{D}\right)^2, \qquad y_r=1000r \tag{3}$$

where A_ℓ and d_ℓ are the effective flow area and equivalent diameter of the leak orifice, respectively, while A_p and D are the cross-sectional area and inner diameter of the main pipeline. Because the original area ratio is small, the scaled area ratio $y_r=1000r$ is used as the regression target during training. The predicted scaled area ratio is then converted into the orifice diameter using Eq. (3).

After preprocessing and label construction, the samples are randomly partitioned in a stratified manner according to each combination of negative-pressure condition, orifice diameter, and leak location. For each of the 48 leakage conditions, the 20 independent samples are divided into training, validation, and test sets at a ratio of 8:1:1, corresponding to 16, 2, and 2 samples, respectively. The resulting sets contain 768, 96, and 96 samples, respectively, with all 48 conditions represented in each set. The training set is used to update the model parameters, the validation set is used for training monitoring and model selection, and the test set is used only for final performance evaluation.

3. Physics-Informed Dual-Stream Decoupling Network

3.1 Multiparameter leakage response mechanisms and overall network architecture

After leakage occurs in a gas drainage pipeline, pressure, flow rate, and oxygen concentration exhibit dynamic responses at different temporal scales. During the initial leakage stage, the negative-pressure disturbance propagates both upstream and downstream. Differences in the transient arrival times and local waveforms among the monitoring nodes provide relative temporal information for estimating the leak location. Leak localization therefore relies primarily on pressure transients measured at multiple nodes and their propagation characteristics. As leakage continues, the pressure and flow rate are gradually redistributed and evolve from the transient state toward a new steady state [19]. In contrast, oxygen concentration exhibits delayed and cumulative changes because of gas transport and mixing. The leak orifice diameter and the pressure difference across the pipe wall jointly determine the leakage flow rate [20]; therefore, the long-term evolution of multiple physical variables provides useful information for orifice diameter estimation.

Leak localization and orifice sizing differ in both their dominant physical variables and response time scales. Modeling the two tasks using a single temporal encoder may cause interference between transient and steady-state features. To incorporate these multiparameter response mechanisms into the network design [21], a physics-informed dual-stream decoupling network (PI-DSDN) is developed. The network contains a transient localization branch and a steady-state sizing branch, which separately encode task-specific features and jointly predict the leak location and orifice diameter through multitask learning. The overall architecture is shown in Fig. 3.

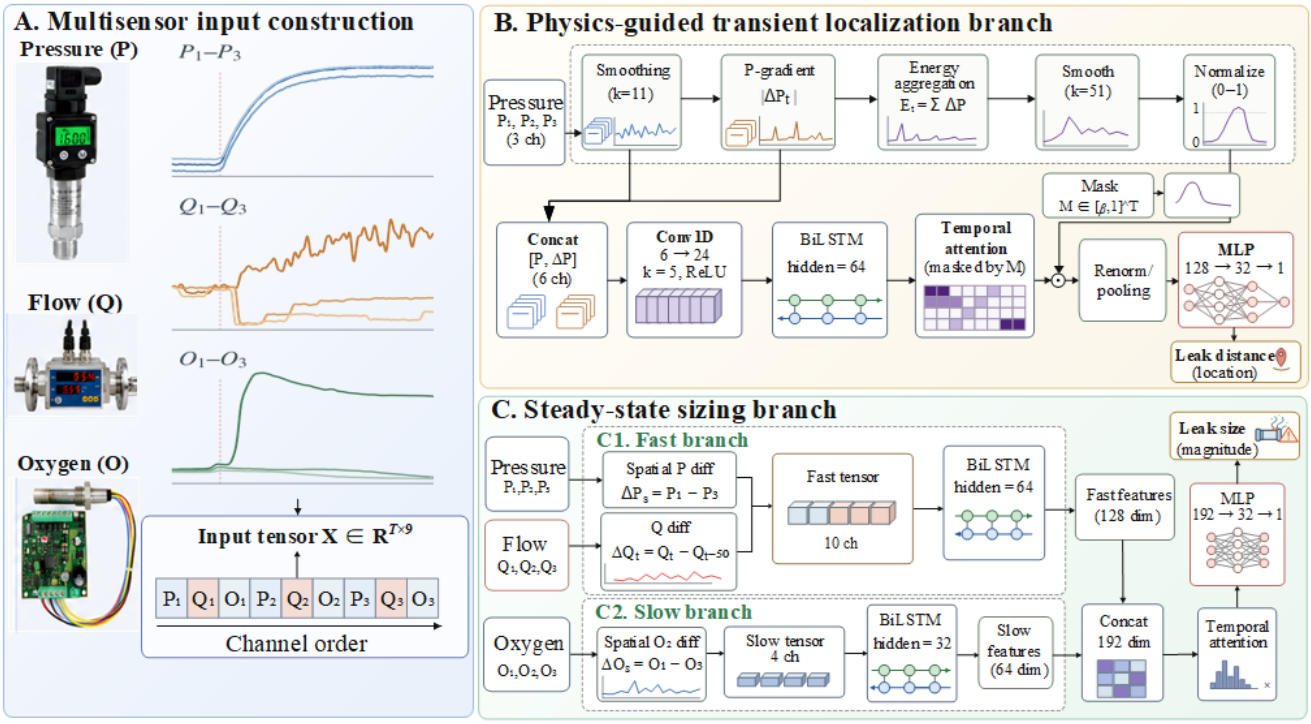


Fig. 3 Overall architecture of the physics-informed dual-stream decoupling network

After physical anchor alignment and baseline correction, the network input is expressed as:

$$\boldsymbol{X} = [\boldsymbol{P}_r, \boldsymbol{Q}_r, \boldsymbol{O}_r] \in \mathbb{R}^{T_w \times N_c} \tag{4}$$

where P_r, Q_r, and O_r denote the pressure, flow-rate, and oxygen-concentration sequences from multiple monitoring nodes, respectively; $T_w = 1750$ is the input window length; and $N_c = 9$ is the number of input channels.

The transient localization branch primarily uses the multipoint pressure sequences. Pressure smoothing and temporal differencing are applied to enhance local transient features, after which a one-dimensional convolutional neural network (1D-CNN) and a bidirectional long short-term memory (BiLSTM) network extract local waveform correlations and relative response timing among the monitoring nodes. A pressure-gradient energy mask is subsequently introduced into the temporal attention mechanism as a physical prior, directing the model toward time regions containing significant leakage transients. The branch finally predicts the relative leak location.

The steady-state sizing branch uses the long-term evolution of pressure, flow rate, and oxygen concentration. These variables are divided into fast- and slow-response groups according to their response rates and are encoded independently. A macroscopic flow-rate difference feature is used exclusively in this branch to characterize post-leakage flow redistribution. The fast and slow temporal features are then fused and weighted using standard temporal attention to predict the leak area ratio. During training, the two branches are jointly optimized using a multitask loss, enabling joint prediction of leak location and orifice diameter while maintaining the separation of task-specific features.

3.2 Physics-guided multiscale transient localization branch

Based on the pressure-transient propagation described above, the transient localization branch uses pressure sequences from multiple monitoring nodes as its input. Smoothed pressure and its absolute first-order difference are employed to represent the disturbance magnitude and local abrupt changes, respectively. A 1D-CNN and a BiLSTM are then used to extract local waveform correlations and relative response timing among the monitoring nodes [22, 23]. Because conventional temporal attention can be affected by operating fluctuations and local noise, the pressure gradients from multiple nodes are further aggregated into an energy mask. This mask serves as a physical prior that constrains attention allocation [24] and directs the model toward time regions containing significant leakage disturbances.

Let $P_{r,n}(t)$ denote the preprocessed pressure sequence at the *nth* monitoring node. Replication padding and moving-average smoothing are applied to suppress local noise:

$$\bar{P}_{r,n}(t) = \frac{1}{K_p} \sum_{k=-m_p}^{m_p} P_{r,n}^{pad}(t+k), \qquad m_p = \frac{K_p - 1}{2} \tag{5}$$

where $\overline{P}_{r,n}(t)$ is the smoothed pressure and K_p is the smoothing-window length. In this study, $K_p = 11$, corresponding to 0.11 s at a sampling frequency of 100 Hz. This window suppresses high-frequency noise while preserving leakage-induced pressure transients.

The absolute first-order difference of the smoothed pressure is then calculated as:

$$\Delta P_{r,n}(t) = \left| \bar{P}_{r,n}(t) - \bar{P}_{r,n}(t-1) \right|, \qquad 2 \le t \le T_w \tag{6}$$

with the difference at the first time step set to zero. The smoothed pressure represents the disturbance magnitude and its temporal evolution, whereas the first-order difference emphasizes local pressure transients and their rates of change. The two features are concatenated along the channel dimension:

$$\boldsymbol{X}_{\text{tr}} = \left[\bar{\boldsymbol{P}}_r, \Delta \boldsymbol{P}_r \right] \in \mathbb{R}^{T_w \times 2N_s} = \mathbb{R}^{T_w \times 6} \tag{7}$$

where $N_s = 3$ is the number of pressure-monitoring nodes. A 1D-CNN subsequently fuses the multipoint pressure correlations within local temporal receptive fields, and a BiLSTM encodes the relative response timing over the complete input window:

$$\boldsymbol{H}_{\mathrm{tr}} = \mathrm{BiLSTM}_{\mathrm{tr}}\left[\phi\left(\mathrm{CNN}_{\mathrm{1D}}\left(\boldsymbol{X}_{\mathrm{tr}}\right)\right)\right] \tag{8}$$

where $\phi(\cdot)$ denotes a nonlinear activation function and $\boldsymbol{H}_{\mathrm{tr}} = [\boldsymbol{h}_1^{loc}, \ldots, \boldsymbol{h}_{T_w}^{loc}]$ is the encoded transient feature sequence.

To reduce interference from operating fluctuations and local noise, the pressure-gradient magnitudes from all monitoring nodes are aggregated into a pressure-gradient energy descriptor:

$$E_t = \sum_{n=1}^{N_s} \Delta P_{r,n}(t) = \sum_{n=1}^{N_s} \left| \bar{P}_{r,n}(t) - \bar{P}_{r,n}(t-1) \right| \tag{9}$$

Here, E_t represents the aggregated pressure-gradient energy at time *t*. Multipoint aggregation combines pressure transients occurring at different pipeline locations and may reduce the influence of local fluctuations at an individual node.

Because a leakage-induced pressure disturbance persists over a finite interval, E_t is locally aggregated and normalized using the maximum value within each sample:

$$\begin{aligned} \bar{E}_t &= \frac{1}{2k+1} \sum_{\tau=-k}^{k} E_{t+\tau} \\ M_t &= \max\left(\beta, \frac{\bar{E}_t}{\max_\tau \bar{E}_\tau + \varepsilon} \right) \end{aligned} \tag{10}$$

where M_t is the pressure-gradient energy mask, k is the half-width of the local temporal window, β is the lower bound of the mask, and ε is a small positive constant. The parameters are set to $k = 25$ and $\beta = 0.01$. Thus, the gradient energy is aggregated over 51 samples, corresponding to 0.51 s. This operation suppresses isolated noise and strengthens persistent pressure disturbances while preventing information in steady-state regions from being completely removed.

Let $\boldsymbol{h}_t^{loc}$ denote the encoded feature at time *t*. Standard temporal attention is first calculated from the transient feature sequence:

$$\begin{aligned} e_t^{loc} &= \boldsymbol{v}_a^{\mathrm{T}} \tanh\left(\boldsymbol{W}_a \boldsymbol{h}_t^{\mathrm{loc}} + \boldsymbol{b}_a \right) \\ a_t^{loc} &= \frac{\exp(e_t^{loc})}{\sum_{\tau=1}^{T_w} \exp(e_\tau^{loc})} \end{aligned} \tag{11}$$

where $\boldsymbol{W}_a$, $\boldsymbol{b}_a$, and $\boldsymbol{v}_a$ are trainable parameters. The base attention is then multiplied by the pressure-gradient energy mask and renormalized:

$$\begin{aligned} \tilde{\alpha}_t^{loc} &= \frac{a_t^{loc} M_t}{\sum_{\tau=1}^{T_w} a_\tau^{loc} M_\tau + \varepsilon} \\ \boldsymbol{g}_{\mathrm{loc}} &= \sum_{t=1}^{T_w} \tilde{\alpha}_t^{loc} \boldsymbol{h}_t^{\mathrm{loc}} \end{aligned} \tag{12}$$

where α_t^{loc} is the physics-guided and renormalized attention weight, and $\mathbf{g}_{\mathrm{loc}}$ is the context feature of the localization branch. Finally, the localization regression head predicts the relative leak location:

$$\hat{y}_{\mathrm{loc}} = f_{\mathrm{loc}}\left(\boldsymbol{g}_{\mathrm{loc}} \right) \tag{13}$$

This mechanism retains the adaptive feature-selection capability of temporal attention while constraining its weight distribution using multipoint pressure-transient information. The pressure-gradient energy mask is applied only to the transient localization branch. Macroscopic flow-rate differences and oxygen-concentration features are excluded from this branch, thereby reducing interference from long-term state evolution in the localization features.

3.3 Steady-state sizing branch based on fast-slow variable decoupling

The leak orifice diameter determines the effective flow area and influences the post-leakage evolution of pressure, flow rate, and oxygen concentration. Pressure and flow rate typically respond relatively rapidly, whereas oxygen concentration exhibits a pronounced delay because of gas transport, mixing, and diffusion. Accordingly, pressure and flow rate are classified as fast-response variables, while oxygen concentration is classified as a slow-response variable. Independent temporal encoders are then employed to extract sizing features at different temporal scales.

To suppress local pulsations in the flow-rate signals, a moving-average window of 51 samples is used to extract the macroscopic flow trend $\bar{Q}_{r,n}(t)$. A macroscopic flow-rate difference with a span of τ is then constructed as:

$$\Delta_\tau \bar{Q}_{r,n}(t) = \bar{Q}_{r,n}(t) - \bar{Q}_{r,n}\left[\max(1, t-\tau)\right], \qquad \tau = 50 \tag{14}$$

At a sampling frequency of 100 Hz, $\tau = 50$ corresponds to 0.5 s. This feature characterizes the post-leakage flow-rate trend and redistribution state.

The pressure and oxygen-concentration differences between the first and last monitoring nodes are further calculated, and the fast- and slow-response feature sets are constructed as:

$$\begin{aligned}
&\delta P^{\mathrm{sp}}(t) = P_{r,1}(t) - P_{r,3}(t) \\
&\delta O^{sp}(t) = O_{r,1}(t) - O_{r,3}(t) \\
&\boldsymbol{X}_{\mathrm{fast}} = [\boldsymbol{P}_r, \boldsymbol{Q}_r, \Delta_\tau \bar{\boldsymbol{Q}}_r, \delta \boldsymbol{P}^{\mathrm{sp}}] \in \mathbb{R}^{T_w \times 10} \\
&\boldsymbol{X}_{\mathrm{slow}} = \left[\boldsymbol{O}_r, \boldsymbol{\delta O}^{\mathrm{sp}}\right] \in \mathbb{R}^{T_w \times 4}
\end{aligned} \tag{15}$$

Here, $\delta P^{\mathrm{sp}}(t)$ and $\delta O^{\mathrm{sp}}(t)$ denote the pressure and oxygen-concentration differences between the first and last monitoring nodes at time *t*, respectively. These spatial differences describe the state variations produced as the leakage disturbance propagates along the pipeline. The macroscopic flow-rate difference is used exclusively in the steady-state sizing branch to strengthen the representation of post-leakage flow redistribution.

The fast- and slow-response sequences are independently encoded using two BiLSTMs with separate parameters:

$$\begin{aligned}
&\boldsymbol{H}^{\mathrm{fast}} = \mathrm{BiLSTM}_{\mathrm{fast}}\left(\boldsymbol{X}_{\mathrm{fast}}\right) \in \mathbb{R}^{T_w \times 128} \\
&\boldsymbol{H}^{\mathrm{slow}} = \mathrm{BiLSTM}_{\mathrm{slow}}\left(\boldsymbol{X}_{\mathrm{slow}}\right) \in \mathbb{R}^{T_w \times 64}
\end{aligned} \tag{16}$$

The fast-response encoder extracts pressure and flow-rate redistribution features, whereas the slow-response encoder represents the delayed and cumulative changes in oxygen concentration. The two hidden-state sequences are subsequently concatenated along the feature dimension and weighted using standard temporal attention:

$$\begin{aligned}
&\boldsymbol{H}_{\mathrm{steady}} = \left[\boldsymbol{H}_{\mathrm{fast}}; \boldsymbol{H}_{\mathrm{slow}}\right] \\
&\boldsymbol{g}_{\mathrm{steady}} = \mathcal{A}_{\mathrm{steady}}\left(\boldsymbol{H}_{\mathrm{steady}}\right)
\end{aligned} \tag{17}$$

where $\mathcal{A}_{\mathrm{steady}}(\cdot)$ denotes standard temporal attention and $\mathrm{g}_{\mathrm{steady}}$ is the fused context feature of the sizing branch. Unlike the transient localization branch, this attention mechanism is not constrained by the pressure-gradient energy mask, allowing the model to learn the temporal features associated with post-leakage state evolution.

Finally, the sizing regression head predicts the leak area ratio scaled by 1000, which is then converted into the actual leak orifice diameter:

$$\hat{y}_r = f_{\text{size}}\left(\boldsymbol{g}_{\text{steady}}\right), \qquad \hat{d}_\ell = D\sqrt{\frac{\hat{y}_r}{1000}} \tag{18}$$

Here, $f_{\text{size}}(\cdot)$ denotes the sizing regression mapping, while $\hat{y}_r$ and $\hat{d}_\ell$ are the predicted scaled leak-area ratio and leak orifice diameter, respectively.

3.4 Multitask joint loss and model training

PI-DSDN simultaneously outputs the predicted relative leak location $\hat{y}_{\text{loc}}$ and the scaled leak-area ratio $\hat{y}_r$, where $\hat{y}_r = 1000\hat{r}$. Because these outputs correspond to two related continuous regression tasks, they are jointly optimized within a multitask learning framework [25]. The localization and sizing losses are defined using the mean squared error:

$$\begin{aligned}\mathcal{L}_{\text{loc}} &= \frac{1}{B}\sum_{n=1}^{B}\left(\hat{y}_{\text{loc},n} - y_{\text{loc},n}\right)^2 \\ \mathcal{L}_{\text{size}} &= \frac{1}{B}\sum_{n=1}^{B}\left(\hat{y}_{r,n} - y_{r,n}\right)^2\end{aligned} \tag{19}$$

where B is the batch size, while $y_{\text{loc},n}$ and $y_{r,n}$ are the relative leak-location label and scaled leak-area-ratio label of the *nth* sample, respectively.

Because the two labels have different numerical scales, their corresponding losses are normalized using the respective label ranges:

$$\begin{aligned}\overline{\mathcal{L}}_{\text{loc}} &= \frac{\mathcal{L}_{\text{loc}}}{\left(\Delta y_{\text{loc}}\right)^2} \\ \overline{\mathcal{L}}_{\text{size}} &= \frac{\mathcal{L}_{\text{size}}}{\left(\Delta y_r\right)^2}\end{aligned} \tag{20}$$

where Δy_{loc} and Δy_r denote the ranges of the two labels in the dataset. The joint multitask loss is then defined as:

$$\mathcal{L} = \lambda_{\text{loc}}\overline{\mathcal{L}}_{\text{loc}} + \lambda_{\text{size}}\overline{\mathcal{L}}_{\text{size}}, \qquad \lambda_{\text{loc}} = \lambda_{\text{size}} = 1 \tag{21}$$

After range normalization, the localization and sizing losses are placed on more comparable scales; therefore, equal weights are used for joint optimization. All models were implemented in Python 3.8 with PyTorch 2.0.1 and trained on an NVIDIA GeForce RTX 3060 GPU. Table 2 lists the main training hyperparameters. Figures were generated using Origin and Matplotlib.

Table 2 Main training hyperparameters of PI-DSDN

Parameter	Value	Parameter	Value
Optimizer	Adam	Batch size	16
Initial learning rate	1.0×10^{-3}	Weight decay	1.0×10^{-4}
Maximum number of epochs	250	LSTM dropout rate	0.2

For the physical-anchor-aligned samples containing 1900 time steps, windows of 1750 samples are randomly cropped in each case during training, whereas fixed windows are used for validation and testing. During training, the learning rate is adjusted according to the joint validation loss, and the model parameters corresponding to the minimum joint validation loss are retained.

4. Results and Discussion

4.1 Evaluation metrics

To comprehensively evaluate the predictive performance of the model for leak localization and orifice diameter estimation, the mean absolute error (MAE), root mean square error (RMSE), and coefficient of determination R^2 are selected as the evaluation metrics. For the localization task, these metrics are calculated using the relative leak location. For the sizing task, they are calculated using the recovered leak orifice diameter in millimeters.

Let z_i and $\hat{z}_i$ denote the true and predicted values of the *ith* sample, respectively, and let N denote the number of evaluated samples. The MAE is defined as:

$$\mathrm{MAE} = \frac{1}{N}\sum_{i=1}^{N}\left|z_i - \hat{z}_i\right| \tag{22}$$

The RMSE is defined as:

$$\mathrm{RMSE} = \sqrt{\frac{1}{N}\sum_{i=1}^{N}\left(z_i - \hat{z}_i\right)^2} \tag{23}$$

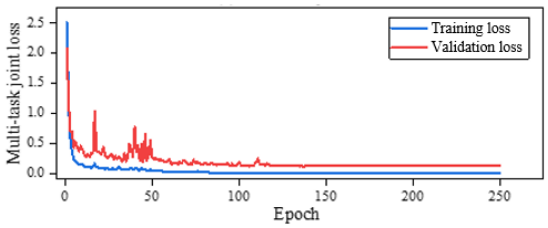
The coefficient of determination is defined as:

$$R^2 = 1 - \frac{\sum_{i=1}^{N}\left(z_i - \hat{z}_i\right)^2}{\sum_{i=1}^{N}\left(z_i - \bar{z}\right)^2} \tag{24}$$

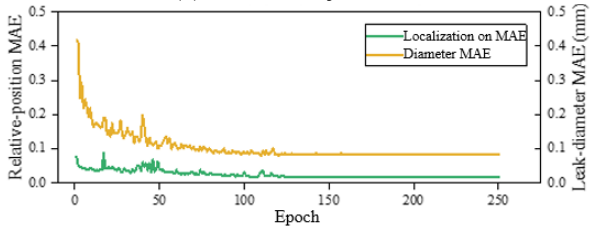
where $\bar{z}$ is the arithmetic mean of the true values. For leak localization, MAE quantifies the average relative-position error, RMSE gives greater weight to large localization errors, and R^2 measures the proportion of variance in leak location explained by the model. For orifice sizing, MAE and RMSE quantify the corresponding diameter errors in millimeters, while R^2 measures the proportion of variance in orifice diameter explained by the model.

4.2 Results of leak localization and orifice diameter estimation

To evaluate the leak localization and orifice diameter estimation performance of PI-DSDN under multiple extraction conditions, the model parameters corresponding to the minimum joint validation loss were selected and used to predict all leakage samples in the independent test set. The normalized multitask joint loss and the prediction errors of the two tasks during training are shown in Fig. 4.



(a) Multi-task joint loss

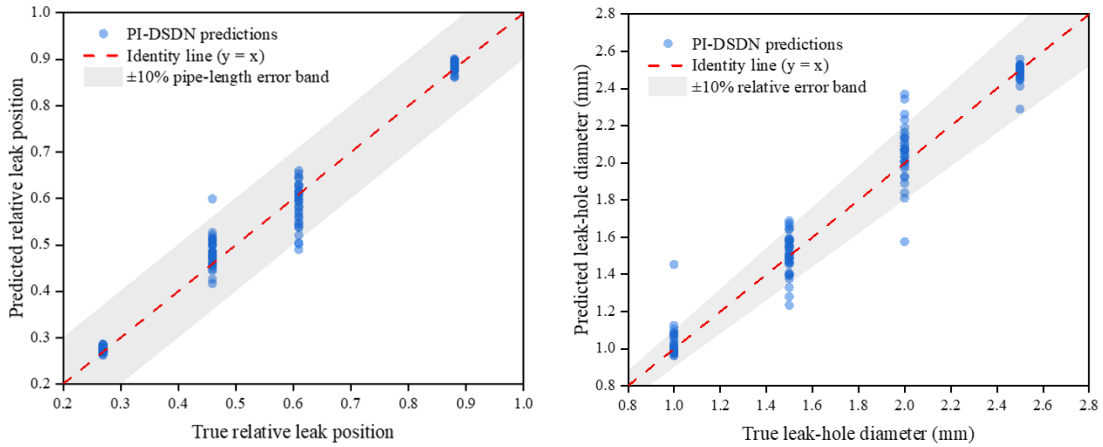


(b) Validation MAE for both tasks

Fig. 4 Training convergence curves of PI-DSDN

As shown in Fig. 4, the training loss and prediction errors decrease rapidly during the initial training stage. Although the validation loss exhibits some fluctuations, it gradually stabilizes as training proceeds, indicating that the model has converged. The model checkpoint corresponding to the minimum joint validation loss is used in all subsequent experiments.

The predicted relative leak locations and orifice diameters are compared with their true values in Fig. 5. The dashed lines represent the identity line, and the shaded regions denote the 10% error reference bands. For localization, the error band is defined relative to the total length of the main pipeline as $|\hat{y}_{\mathrm{loc}} - y_{\mathrm{loc}}| \leq 0.10$, corresponding to a localization tolerance of ±10% of the total pipeline length. For orifice diameter estimation, the error band is defined relative to the true diameter as $0.9d_l \leq \hat{d}_l \leq 1.1d_l$. Because the experimental design contains four discrete leak locations and four discrete orifice diameters, the true values appear as distinct groups in the scatter plots. The quantitative results obtained on the test set are summarized in Table 3.



(a) Leak localization (b) Leak-hole diameter estimation

Fig. 5 PI-DSDN predictions on the test set

Table 3 Leak localization and orifice diameter estimation performance of PI-DSDN on the test set

Prediction task	MAE	RMSE	R^2
Leak localization	0.0218	0.0342	0.9754
Orifice diameter estimation	0.0736 mm	0.1129 mm	0.9566

For leak localization, the predicted values are generally concentrated around the identity line. The localization MAE of 0.0218 corresponds to 2.18% of the total pipeline length, or approximately 0.283 m for the 13 m pipeline, indicating that the transient localization branch effectively extracts multipoint pressure transients and relative response timing associated with different leak locations.

For orifice diameter estimation, the predictions at different diameter levels are also distributed close to the identity line. The diameter MAE is 0.0736 mm, demonstrating that the steady-state sizing branch can integrate the multiscale evolution of pressure, flow rate, and oxygen concentration to estimate the leak orifice diameter.

The RMSE values for both tasks are higher than their corresponding MAEs. As shown in Fig. 5, only a small number of test samples deviate from the identity line, and the overall prediction errors remain low. Overall, PI-DSDN demonstrates stable joint regression performance for the four leak locations and four orifice diameters considered on the 13 m PVC experimental platform. Future work will conduct cross-platform validation and extend the current single-leak model to multiple-leak scenarios using multiple-leak samples and multi-target outputs.

4.3 Comparison with baseline models

To evaluate the ability of PI-DSDN to model heterogeneous multiparameter time-series features, 1D-CNN, standard BiLSTM, and CNN-LSTM are selected as baseline models. The 1D-CNN primarily extracts local variations from the time-

series signals, the BiLSTM models bidirectional temporal dependencies, and the CNN-LSTM combines local convolutional feature extraction with long-term temporal encoding. All models use the same dataset partition, input data, training settings, and evaluation metrics for the localization and sizing tasks. Their performance on the test set is summarized in Table 4.

Table 4 Leak localization and orifice diameter estimation performance of different models on the test set

Model	Localization R^2	Localization MAE	Localization RMSE	Sizing R^2	Sizing MAE (mm)	Sizing RMSE (mm)
1D-CNN	0.8712	0.0617	0.0783	0.8180	0.1682	0.2312
Standard BiLSTM	0.9311	0.0440	0.0573	0.6834	0.2244	0.3049
CNN-LSTM	0.9413	0.0398	0.0499	0.8908	0.1341	0.1850
PI-DSDN	0.9754	0.0218	0.0342	0.9566	0.0736	0.1129

As shown in Table 4, PI-DSDN achieves the highest R^2 and the lowest prediction errors for both tasks. Compared with CNN-LSTM, the best-performing baseline model, PI-DSDN reduces the localization MAE and RMSE by 45.2% and 31.5%, respectively. For orifice diameter estimation, R^2 increases from 0.8908 to 0.9566, corresponding to an absolute improvement of 0.0658, while the MAE and RMSE decrease by 45.1% and 39.0%, respectively. These results indicate that PI-DSDN provides more accurate predictions by combining multipoint pressure-transient information with post-leakage multiparameter evolution and macroscopic flow redistribution relevant to orifice diameter estimation.

The 1D-CNN captures local temporal variations but may have limited ability to represent long-term state evolution. The standard BiLSTM performs relatively well in localization but achieves an R^2 of only 0.6834 for diameter estimation. This result suggests that directly feeding fast- and slow-response variables into a single temporal encoder may be insufficient to represent diameter-related information at different temporal scales. CNN-LSTM improves the overall performance by combining local convolutional feature extraction with temporal encoding; however, it lacks task-specific feature decoupling and explicit physical-prior guidance.

In contrast, PI-DSDN uses the transient localization and steady-state sizing branches to model leakage responses at different temporal scales. The pressure-gradient energy mask directs the localization branch toward time regions containing significant pressure transients, while the macroscopic flow-rate difference provides the sizing branch with information on post-leakage flow redistribution. These task-specific mechanisms contribute to the joint prediction performance in both regression tasks. Their individual contributions are further examined through the ablation study in the following section.

4.4 Ablation study

A 2 × 2 factorial ablation study is conducted to evaluate the contributions of the pressure-gradient energy mask and the macroscopic flow-rate difference. Model A is the baseline model, which retains the dual-stream encoding architecture and standard temporal attention but excludes both physics-informed components. Model B incorporates only the pressure-gradient energy mask, while Model C incorporates only the macroscopic flow-rate difference. The complete PI-DSDN contains both components. All models use the same data and training settings. Their test-set results are presented in Table 5.

Table 5 Leak localization and orifice diameter estimation performance of different ablation models on the test set

Model	Localization R^2	Localization MAE	Localization RMSE	Sizing R^2	Sizing MAE (mm)	Sizing RMSE (mm)
Model A (Baseline)	0.9157	0.0385	0.0527	0.9027	0.1257	0.1655
Model B (MaskOnly)	0.9659	0.0248	0.0381	0.9087	0.1218	0.1593
Model C (FlowOnly)	0.9182	0.0372	0.0561	0.9487	0.0885	0.1595
PI-DSDN	0.9754	0.0218	0.0342	0.9566	0.0736	0.1129

As shown in Table 5, introducing the pressure-gradient energy mask increases the localization R^2 of Model B from 0.9157 to 0.9659 relative to Model A, while reducing the localization MAE and RMSE by 35.6% and 27.7%, respectively. In contrast, its sizing metrics change only slightly. These results indicate that the pressure-gradient energy mask constrains the attention distribution using multipoint pressure-transient information and directs the localization branch toward time regions containing significant leakage disturbances, thereby improving the extraction of relative response timing.

When only the macroscopic flow-rate difference is introduced, the localization performance of Model C remains comparable to that of Model A. However, its sizing R^2 increases from 0.9027 to 0.9487, and the sizing MAE decreases by 29.6%. This result demonstrates that the macroscopic flow-rate difference effectively characterizes post-leakage flow redistribution and improves the overall prediction accuracy of the steady-state sizing branch. Nevertheless, the sizing RMSE decreases by only 3.6%, indicating that this feature alone provides limited improvement for the small number of samples with relatively large diameter errors.

The complete PI-DSDN, which incorporates both physics-informed components, achieves the best performance in both tasks. Compared with Model A, it reduces the localization MAE and RMSE by 43.4% and 35.1%, respectively, and the sizing MAE and RMSE by 41.4% and 31.8%, respectively. The ablation results demonstrate that the pressure-gradient energy mask and macroscopic flow-rate difference primarily contribute to transient localization and steady-state sizing, respectively. The two components therefore exhibit clear task selectivity and provide complementary information through the dual-stream decoupling architecture.

To further investigate the effect of physical priors on feature selection, a representative sample with a relative leak location of 0.27 is selected, and the localization and sizing attention distributions of the four models are visualized in Figs. 6 and 7, respectively. The gray dashed line indicates the leakage onset, and the background color intensity represents the attention strength. The background color in each panel is normalized independently and is used only to illustrate the relative temporal distribution of attention within a single model. Quantitative comparisons among the models are performed directly using the original attention weights output by each model, which are normalized along the temporal dimension and sum to 1. Based on the pressure-transient and subsequent evolution stages of the selected sample, the proportions of attention assigned to the 4-6 s transient interval and the 6-17.5 s long-term evolution interval are calculated.

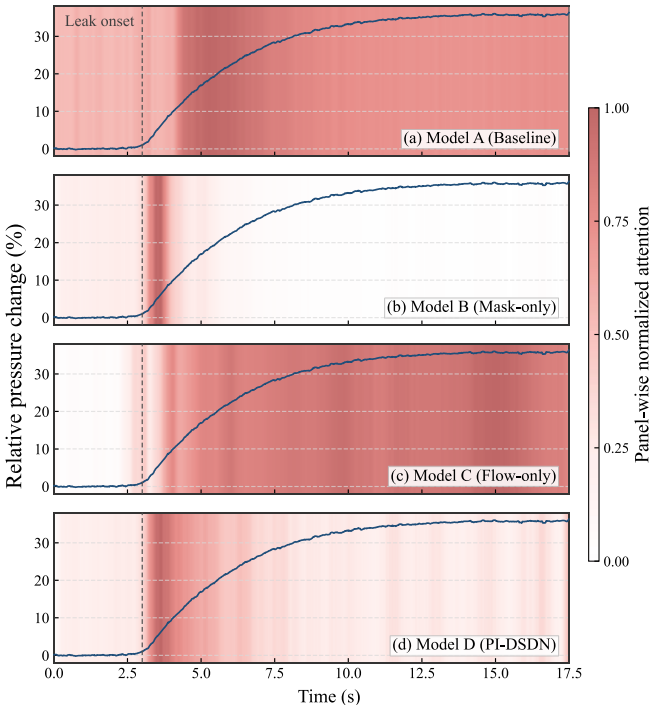


Fig. 6 Temporal-attention distributions of the localization branch for different ablation models

As shown in Fig. 6, Models A and C, which exclude the pressure-gradient energy mask, maintain relatively diffuse attention over an extended period after leakage and do not clearly emphasize the transient interval relevant to localization. After the energy mask is introduced, the high-attention regions of Model B and PI-DSDN become concentrated around the initial pressure-transient stage. Based on the model-output attention weights before visualization normalization, the proportion of total localization attention assigned to the 4-6 s transient interval increases from 11.65% in Model A to 18.85% in Model B and from 11.55% in Model C to 17.83% in PI-DSDN, corresponding to relative increases of 61.8% and 54.3%, respectively. These results quantitatively demonstrate that the energy mask directs localization attention toward leakage transients and improves the identification of pressure-transient timing.

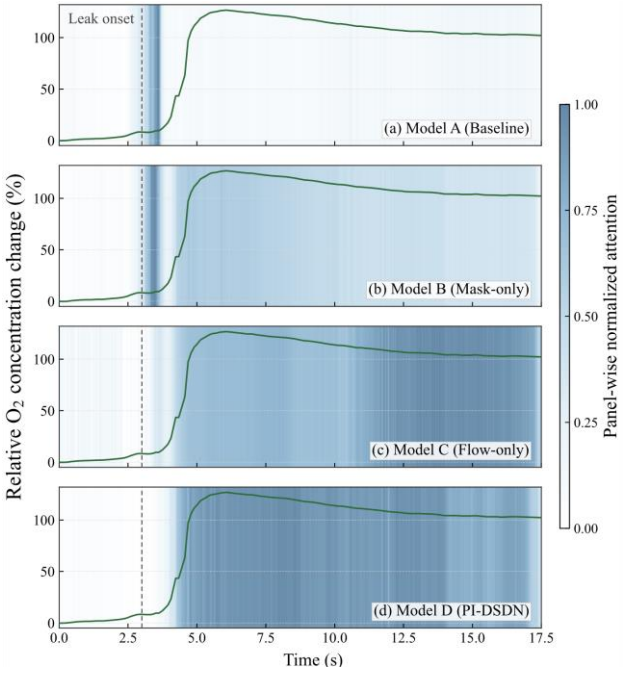


Fig. 7 Temporal-attention distributions of the sizing branch for different ablation models

As shown in Fig. 7, Models A and B, which exclude the macroscopic flow-rate difference, focus mainly on the initial leakage stage and assign relatively limited attention to the subsequent state evolution. After this feature is introduced, Model C and PI-DSDN exhibit a more continuous high-attention distribution over the extended post-leakage interval. Within the 6-17.5 s long-term evolution interval, the proportion of total sizing attention increases from 63.05% in Model A to 78.35% in Model C and from 70.91% in Model B to 82.91% in PI-DSDN, corresponding to relative increases of 24.3% and 16.9%, respectively. These results indicate that the macroscopic flow-rate difference strengthens the use of post-leakage flow redistribution and long-term state-evolution information by the sizing branch.

Taken together, the quantitative results and attention distributions show that the pressure-gradient energy mask primarily strengthens transient localization features, whereas the macroscopic flow-rate difference mainly enhances steady-state sizing features. Each physical prior acts on its corresponding task branch, supporting the rationale for the dual-stream decoupling design of PI-DSDN. The relationship between the attention distributions of the complete model and the multipoint physical responses is examined further in Section 4.5.

4.5 Interpretability analysis of temporal attention

Temporal-attention weights indicate the relative importance assigned by a model to information at different time steps and therefore provide a degree of temporal interpretability [26]. To investigate how the two branches of PI-DSDN select information at different temporal scales, a representative sample with a relative leak location of 0.27 is selected. The temporal-attention distributions of the complete model are visualized together with the pressure, flow-rate, and oxygen-concentration responses measured at the three monitoring nodes, as shown in Fig. 8.

The left column presents the physics-guided temporal attention of the localization branch, while the right column presents the standard temporal attention of the sizing branch. A darker background indicates a higher attention weight at the corresponding time step. The three panels in each column use the same attention sequence, and the physical signals are superimposed to examine their temporal correspondence with the attention distributions. The color scales of the two columns are set independently and therefore should not be used to compare the absolute attention magnitudes of the two branches.

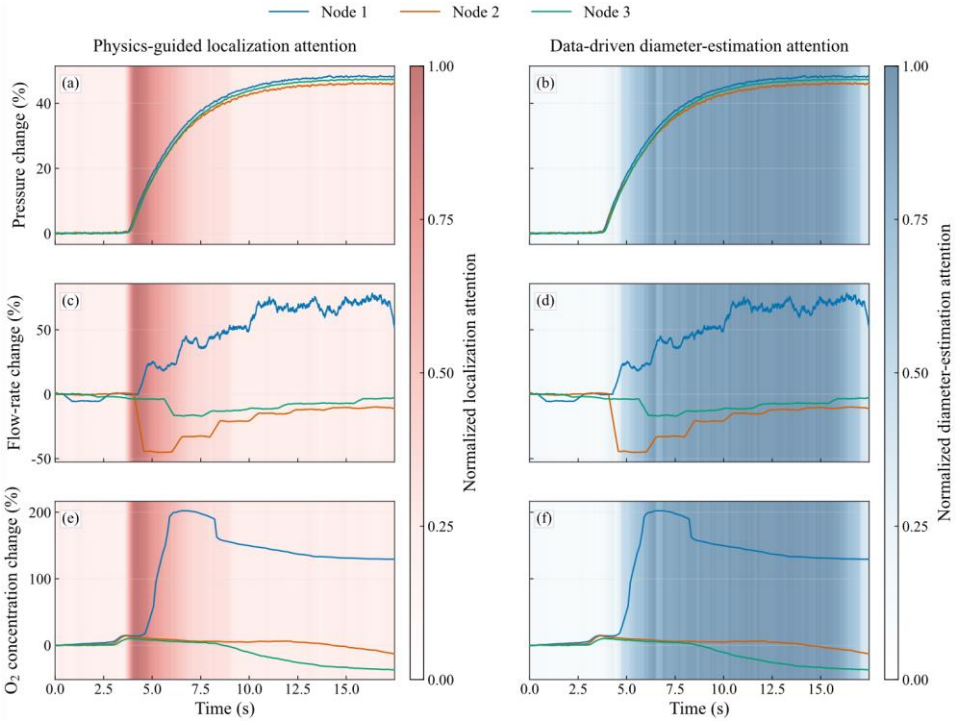


Fig. 8 Correspondence between the dual-branch temporal attention of PI-DSDN and multipoint physical responses

As shown in Figs. 8(a), 8(c), and 8(e), the monitored signals remain relatively stable before leakage, and the localization branch assigns low attention weights to this interval. After leakage causes rapid pressure changes, the localization attention increases markedly during the transient-response interval of approximately 4-6 s and decreases as the system enters the subsequent evolution stage. This high-attention interval generally coincides with the onset of rapid pressure changes at the monitoring nodes, as well as the initial stages of flow redistribution and oxygen-concentration response. This correspondence is consistent with the intended role of the pressure-gradient energy mask in emphasizing leakage-induced local transients and response timing relevant to leak localization. It also suggests that the localization branch places less emphasis on subsequent long-term state changes.

In contrast, the sizing attention shown in Figs. 8(b), 8(d), and 8(f) gradually increases during the initial leakage stage and remains relatively high over an extended interval after approximately 6 s. During this period, the pressure signals gradually approach a new steady state, the flow rates undergo sustained redistribution, and the oxygen concentrations exhibit pronounced cumulative changes and long-term tail responses. With the assistance of the macroscopic flow-rate difference, the sizing branch can use standard temporal attention to integrate long-term post-leakage state information and extract leakage-induced mass-flow loss and steady-state response features associated with the orifice diameter.

Taken together, the ablation metrics, attention-weight proportions, and visualizations in Fig. 8 reveal a clear difference in temporal scale between the two task branches of PI-DSDN. The localization branch focuses primarily on the transient-change interval after leakage onset, whereas the sizing branch emphasizes the subsequent sustained evolution and steady-state response. This feature-selection pattern is consistent with the task-specific physical information used by the two branches, providing quantitative and visual evidence for the dual-stream decoupling architecture and physics-guided attention in leak localization and orifice diameter estimation.

5. Conclusions

This study developed a physics-informed dual-stream decoupling network (PI-DSDN) for the joint localization and orifice diameter estimation of leaks in gas drainage pipelines. The pressure-gradient energy mask was used to strengthen transient localization features, while fast-slow variable decoupling and a macroscopic flow-rate difference were employed to characterize post-leakage steady-state evolution for orifice sizing. The main conclusions are summarized as follows.

(1) For leak localization, PI-DSDN achieved an R^2 of 0.9754, an MAE of 0.283 m, and an RMSE of 0.445m; for orifice diameter estimation, it achieved an R^2 of 0.9566, an MAE of 0.0736 mm, and an RMSE of 0.1129 mm. Compared with CNN-LSTM, the localization and sizing MAEs were reduced by 45.2% and 45.1%, demonstrating improved joint prediction performance across the tested combinations of vacuum-pump power, leak location, and orifice diameter.

(2) The ablation and attention analyses showed that the pressure-gradient energy mask primarily directs the localization branch toward leakage-induced pressure transients, whereas the macroscopic flow-rate difference enables the sizing branch to make greater use of long-term post-leakage state evolution. These task-specific effects support the dual-stream decoupling architecture and improve the physical interpretability of the model.

Future studies will evaluate the generalizability of PI-DSDN using more complex pipeline-network configurations, stronger operating noise, and field measurements. Particular attention will be given to previously unseen operating conditions and simultaneous leaks at multiple locations.

Acknowledgment

This work was supported by the Key Research and Development Program of Shaanxi Province (Grant No. 2022QCY-LL-70) and the Qin Chuangyuan “Scientist + Engineer” Team Development Program of Shaanxi Province (Grant No. 2023KXJ-052).

Conflicts of Interest

The authors declare no conflict of interest.

References

[1] L. Wang, Y. Sun, S. Zheng, L. Shu, and X. Zhang, “How Efficient Coal Mine Methane Control Can Benefit Carbon-Neutral Target: Evidence from China,” Journal of Cleaner Production, vol. 424, article no. 138895, 2023.

[2] J. Sekhavati, S. H. Hashemabadi, and M. Soroush, “Computational Methods for Pipeline Leakage Detection and Localization: A Review and Comparative Study,” Journal of Loss Prevention in the Process Industries, vol. 77, article no. 104771, 2022.

[3] H. Zhang, M. Shen, Z. Huo, Y. Zhang, L. Shu, and Y. Li, “Research on Gas Drainage Pipeline Leakage Detection and Localization Based on the Pressure Gradient Method,” Processes, vol. 12, no. 8, article no. 1590, 2024.

[4] R. Xiao and J. Li, “Evaluation of Acoustic Techniques for Leak Detection in a Complex Low-Pressure Gas Pipeline Network,” Engineering Failure Analysis, vol. 143, part A, article no. 106897, 2023.

[5] W. Gan, Y. Zhang, S. Jia, R. Luo, J. Tang, and C. Zhang, “UWFBG Array Vibration Sensing Technology for Gas Pipeline Leakage Detection and Location,” Optics Communications, vol. 560, article no. 130414, 2024.

[6] R. Ma, J. Liu, W. Wu, Y. Yang, X. Liu, S. Zhang, et al., “Minor Pipeline Leak Detection and Localization Using Explainable Deep Learning with Fusion of Distributed Fiber-Optic Vibration and Temperature Signals,” Journal of Loss Prevention in the Process Industries, vol. 100, article no. 105844, 2026.

[7] Z. Zuo, L. Ma, S. Liang, J. Liang, H. Zhang, and T. Liu, “A Semi-Supervised Leakage Detection Method Driven by Multivariate Time Series for Natural Gas Gathering Pipeline,” Process Safety and Environmental Protection, vol. 164, pp. 468–478, 2022.

[8] J. Zhou, H. Lin, S. Li, H. Jin, B. Zhao, and S. Liu, "Leakage Diagnosis and Localization of the Gas Extraction Pipeline Based on SA-PSO BP Neural Network," Reliability Engineering & System Safety, vol. 232, article no. 109051, 2023.

[9] J. Zhou, W. Zhang, J. Zhao, J. Ge, W. Li, and J. Liu, "Research on Multi-Source Collaborative Leakage Location Method for Coal Mine Gas Extraction Pipeline Based on Stacking Integration Learning," Processes, vol. 14, no. 12, article no. 1908, 2026.

[10] X. Zhang, J. Shi, M. Yang, X. Huang, A. S. Usmani, G. Chen, et al., "Real-Time Pipeline Leak Detection and Localization Using an Attention-Based LSTM Approach," Process Safety and Environmental Protection, vol. 174, pp. 460–472, 2023.

[11] J. Liang, S. Liang, L. Ma, H. Zhang, J. Dai, and H. Zhou, "Leak Detection for Natural Gas Gathering Pipeline Using Spatio-Temporal Fusion of Practical Operation Data," Engineering Applications of Artificial Intelligence, vol. 133, part D, article no. 108360, 2024.

[12] P. Li, X. Wang, C. Jiang, H. Bi, Y. Liu, W. Yan, et al., "Advanced Transformer Model for Simultaneous Leakage Aperture Recognition and Localization in Gas Pipelines," Reliability Engineering & System Safety, vol. 241, article no. 109685, 2024.

[13] C. Wu, H. Lu, D. Liu, C. Wang, J. Gan, and Z. Li, "Research on Gas Pipeline Leakage Prediction Model Based on Physics-Aware GL-TransLSTM," Biomimetics, vol. 10, no. 11, article no. 743, 2025.

[14] N. J. H. Keumoe, A. Singh, I. Srivastava, B. Shinganand, and D. M. Mahapatra, "Methane Leak Detection in Natural Gas Pipelines and City Gate Stations Using an AI/ML-Integrated Simulation Framework," Hydrogen Economy & Engineering, article no. 100010, 2026.

[15] Q. Jing, X. Song, B. Sun, Y. Li, and L. Zhang, "Efficient Estimation of Natural Gas Leakage Source Terms Using Physical Information and Improved Particle Filtering," Reliability Engineering & System Safety, vol. 260, article no. 110989, 2025.

[16] K. R. Rahman, A. Khandakar, A. Barooah, M. A. Ayari, and M. A. Rahman, "Multiphase System Leak Detection, Localization, and Dimension Estimation Using Multi-Head Physics-Informed Neural Network," Process Safety and Environmental Protection, vol. 211, article no. 108532, 2026.

[17] O. M. Ibrahim, J. Shin, R. Sikka, P. M. Hansen, and K. Vaagsaether, "Experimental Study on Hydrogen Pipeline Leakage: Negative Pressure Wave Characteristics and Inline Detection Method," Journal of Loss Prevention in the Process Industries, vol. 92, article no. 105452, 2024.

[18] Y. Wang, W. Liu, Q. Zhang, L. Feng, and W. Liu, "Gas Pipeline Leakage Detection and Localization Method Based on VMD-DTW," Flow Measurement and Instrumentation, vol. 102, article no. 102820, 2025.

[19] J. Kim, S. Han, D. Kim, and Y. Lee, "Gas Pipeline Leak Detection by Integrating Dynamic Modeling and Machine Learning under the Transient State," Energies, vol. 17, no. 21, article no. 5517, 2024.

[20] B. Ayyildiz, M. Z. Sheriff, M. A. Rahman, A. Delgado, I. Hassan, H. Nounou, et al., "Research on Pinhole Accidental Gas Release in Pipelines: Statistical Modeling, Real Gas CFD Simulation, and Validation," Process Safety and Environmental Protection, vol. 176, pp. 786–796, 2023.

[21] A. Karpatne, G. Atluri, J. H. Faghmous, M. Steinbach, A. Banerjee, A. Ganguly, et al., "Theory-Guided Data Science: A New Paradigm for Scientific Discovery from Data," IEEE Transactions on Knowledge and Data Engineering, vol. 29, no. 10, pp. 2318–2331, 2017.

[22] A. Graves and J. Schmidhuber, "Framewise Phoneme Classification with Bidirectional LSTM and Other Neural Network Architectures," Neural Networks, vol. 18, nos. 5-6, pp. 602–610, 2005.

[23] D. Yan, G. Wang, J. Wang, L. Ren, and Z. Jia, "Pipeline Multi-Point Leakage Identification Based on Temporal Convolutional Network," Flow Measurement and Instrumentation, vol. 106, article no. 102992, 2025.

[24] G. E. Karniadakis, I. G. Kevrekidis, L. Lu, P. Perdikaris, S. Wang, and L. Yang, "Physics-Informed Machine Learning," Nature Reviews Physics, vol. 3, no. 6, pp. 422–440, 2021.

[25] R. Caruana, "Multitask Learning," Machine Learning, vol. 28, no. 1, pp. 41–75, 1997.

[26] W. Pei, T. Baltrušaitis, D. M. J. Tax, and L.-P. Morency, "Temporal Attention-Gated Model for Robust Sequence Classification," Proceedings of the 2017 IEEE Conference on Computer Vision and Pattern Recognition (CVPR), pp. 820–829, 2017.



Copyright© by the authors. Licensee TAETI, Taiwan. This article is an open access article distributed under the terms and conditions of the Creative Commons Attribution (CC BY-NC) license (https://creativecommons.org/licenses/by-nc/4.0/).